An Energy Injection Method to Improve Power Transfer Capability of Bidirectional WPT System With Multiple Pickups

Xin Dai, *Member, IEEE*, Jinde Wu, Jincheng Jiang, Ruozhong Gao, and Udaya K. Madawala, *Fellow, IEEE*

***Abstract*—Track wireless power transfer (WPT) systems are increasingly used for monorail robots, industrial transportation, etc. Conventionally, the track WPT system's primary power supply is designed to be equal or higher than the total running pickups' rated power. However, in practice, some of the pickups may transiently require more power than their normal operating state. It is not cost effective to increase the power rating of the primary source for the transient case. Hence, this article proposes a method to strengthen the track's power transfer capability by reversely injecting energy from available online pickups to the transiently over-rated one. A bioperation mode is proposed, which includes both the normal operation and the strengthening operation. A bidirectional pickup topology is used, and the equivalent circuit is analyzed accounting the bioperation mode. In addition, a synchronization method of the primary and reverse injection pickups is proposed. A criterion to determine the boundary of the reverse energy injection is also presented. By detecting the peak current, this energy injection method can be practically implemented and the proposed method is verified through the experimental results.**

***Index Terms*—Power transfer capability strengthening method, reverse energy injection, synchronization, wireless power transfer.**

NOMENCLATURE

Symbol	Description
$U_{\rm dc}$, $U_{{\rm dc}(i)}$	Input voltage of primary and pickup inverter.
$U_{\rm ac}$, $U_{{\rm ac}(i)}$	Output voltage rms of primary and pickup inverter.
E_i	Battery voltage.
L_{pi}, $L_{so(i)}$	Inductance of *LCL* resonant network in primary and pickup.
L_p, L_T, $L_{s(i)}$	Self-inductance of primary coil, track coil, and pickup coil.
M, M_i	Mutual inductance between primary coil and track coil, and mutual inductance between pickup coil and track coil.
C_p, C_T, $C_{s(i)}$	Resonant capacitance of primary, track, and pickup.
R_i, $R_{l(i)}$	Load impedance and equivalent ac impedance.
I_p, I_t, $I_{s(i)}$, $I_{so(i)}$	Current rms in primary coil, track coil, pickup coil, and pickup inductance.
f, ω	Operating frequency and angular frequency.
$Z_{s(i)}$	Total impedance of forward receiving pickup.
Z_t	Total impedance of track .
U_{tp}, $U_{t(i)}$ $U_{s(i)}$	Induced voltage of track coil and pickup coil.
$U_{o(i)}$	Output voltage rms of the equivalent ac load.
$U_{{\rm out}(i)}$	Output voltage of the load.
$P_{o(i)}$	Output power.

Manuscript received November 27, 2019; revised March 30, 2020, June 24, 2020, and September 6, 2020; accepted October 12, 2020. Date of publication October 21, 2020; date of current version January 22, 2021. This work was supported in part by the research funds for the National Natural Science Foundation of China under Grant 51777022 and in part by the China National Center for International Research on Wireless Power Transfer Technologies. Recommended for publication by Associate Editor J. M. R. Daliva. *(Corresponding author: Xin Dai.)*

Xin Dai, Jinde Wu, Jincheng Jiang, and Ruozhong Gao are with the School of Automation, Chongqing University, Chongqing 400044, China (e-mail: toybear@vip.sina.com; 376492330@qq.com; 704020211@qq.com; 782452614@qq.com).

Udaya K. Madawala is with the Department of Electrical and Computer Engineering, University of Auckland, Auckland 1010, New Zealand (e-mail: u.madawala@auckland.ac.nz).

Color versions of one or more of the figures in this article are available online at https://ieeexplore.ieee.org.

Digital Object Identifier 10.1109/TPEL.2020.3032676

I. INTRODUCTION

WIRELESS power transfer (WPT) technology realizes energy transmission across an air gap between a power source and the receiving devices. It is efficient, convenient, safe, and able to provide good reliability in harsh environments [1], [2]. The WPT technology can be used in different applications such as biomedical implants [3], [4], consumer electronics [5], and electric vehicles [6], [7].

Track WPT systems transfer energy wirelessly for multiple receivers by a long track coil. They can be used for monorail robots, industrial transportation, etc. In practice, a moving vehicle may require a transient large power input that exceeds its normal operating state. Unlike the conventional wired power supply, power transfer capability of the WPT system considerably relies on the power rating of the primary source [8], [9]. Additionally, if a track system is designed to meet all transient power requirements, it might not be economically viable. Therefore, it is desirable to dynamically strengthen the track's power transfer capability to address this problem without significantly increasing the system size or cost.

Recent progresses in track WPT system are mainly on improving the system efficiency with reduced cost. The work in [10] presents a *dq*-power supply rail charged by two high-frequency ac currents of the *d*-phase and *q*-phase to make the pickup induced voltage spatially uniform. The work in [11] presents

a novel magnetic coupling mechanism with constant output and lower construction cost. In comparison to the conventional I-type power supply rail, the n-type power supply rail improves the utilization of the magnetic core. New cross-segmented power supply rails are proposed in [12] for roadway-powered electric vehicles, which can reduce the construction cost and electromagnetic field. A novel coupler topology is proposed in [13], which facilitates large tolerance on horizontal misalignment. In [14], the primary with various multiple-coil-pad designs is investigated, and the system can switch between various excitation modes during operation, without tuning or additional adjustments. The work in [15] sets up a WPT charging system that uses a series of sectional primary coils, and the system can reduce the loss and enhance the transfer efficiency.

For the WPT system with multiple pickups, current research works mainly focus on improving the system stability. The work in [16] provides a general analysis on multiple-receiver WPT systems and a compensation accounting the influence of the cross coupling. In [17], the output voltage characteristics of a multiple-receiver WPT system against load variations are studied, and the operating frequency to achieve a constant output voltage is determined. The work in [18] proposes the conditions to achieve maximum transmission efficiency and maximum output power for a multiload system. Regarding the stability of the multiload mode, the work in [19] studies the influence of the number of loads to the system stability and defines the boundary condition of the load quantity.

The system proposed in [20] is suitable for wireless and simultaneous charging/discharging of multiple electric vehicle (EVs) or other equipment. The study also establishes a mathematical model of the system and focuses on the method to control the amount and the direction of the power flow between the EVs/equipment and grid. To reduce the voltage and current ratings of the available semiconductor devices in high-power WPT system, a ring WPT system with an intermediate *LCL* circuit is proposed in [21]. The results show that the method presented in [21] is ideal for high-power applications. In summary, current research works on track WPT systems and multiple pickups are mainly associated with the coupling mechanism and system efficiency. There are limited numbers of publications discussing the improvement of track power transfer capability.

This article proposes a track power transfer capability strengthening method by reverse energy injection from other online pickups to the pickup that is transiently overrated. The track WPT system can be designed under a bioperation mode: 1) normal mode, in which the primary supply the power for all the pickups; and 2) strengthening mode, in which some of the pickup modules together with the primary supply power to the pickup module that transiently overrated. In addition, a synchronization method of the primary source and reverse injection pickup sources is proposed. Furthermore, to determine the control algorithm for the energy strengthening mode, a boundary condition is applied for the reverse energy injection.

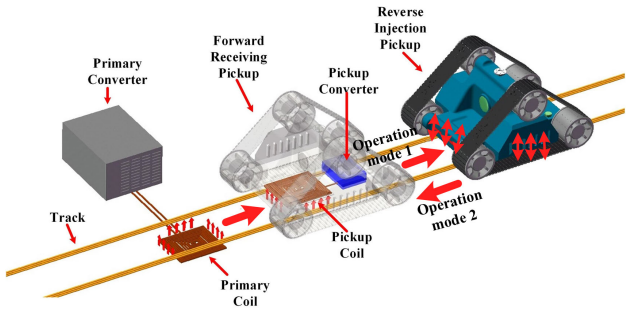

Fig. 1. Proposed track WPT system.

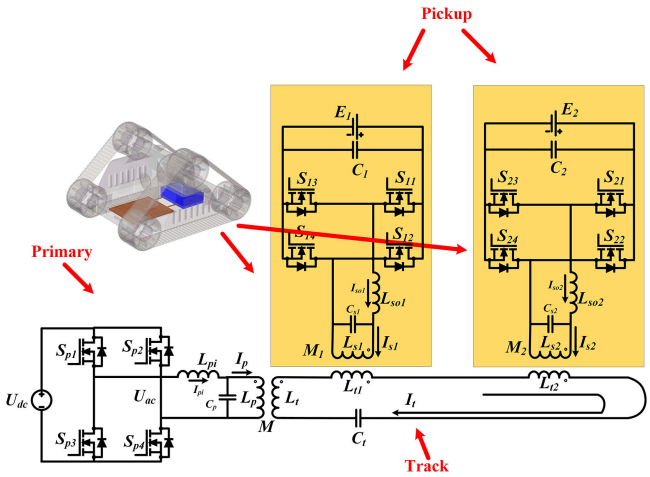

Fig. 2. Schematic diagram of the proposed track WPT system.

II. Two Power Transfer Modes for Track WPT System With Multiple Pickups

Generally, a track WPT system is equipped with multiple pickups to meet the requirements of multiple moving devices. The topology of such system and two types of power transfer modes are presented in Fig. 1.

Fig. 2 shows a typical track WPT system with multiple pickups. At the primary side, the dc input voltage source is expressed as U_{dc}. A high-frequency inverter operating at a fixed frequency generates a square-wave voltage source driving the resonant tank. In the resonant stage, *LCL* resonant topology is composed by L_{pi}–C_p–L_p. The track coil is coupled with multiple pickups, and the pickups can move freely along the track coil. To keep the constant currents of the primary coil and the reverse-injection pickup coils, *LCL* topology is chosen at the primary side and the pickup sides. The resonant frequencies of the *LCL* topology and *LC* topology are independent of the load and the mutual inductance.

To facilitate energy exchange between the track and the pickups, each pickup can switch its operation mode between the normal mode and the strengthening mode. In the normal mode, the pickup obtains energy from the track and charges the battery of the robot. In the strengthening mode, the battery with excess energy reversely injects energy into the track coil and enhances its power transfer capability.

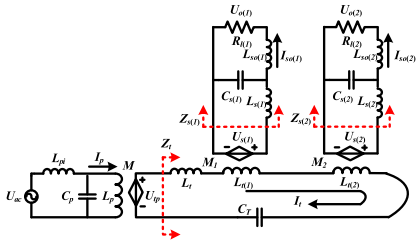

Fig. 3. Equivalent circuit of the operation mode 1.

To facilitate the analysis of the two operation modes, it is necessary to provide a few fundamental definitions. When the pickup works in the strengthening mode, the relation between the dc voltage $U_{\mathrm{dc}(i)}$ and inverter output voltage $U_{\mathrm{ac}(i)}$ is similar to that between U_{dc} and U_{ac} at the primary side, which is given by

$$U_{\mathrm{ac}}=\frac{2\sqrt{2}U_{\mathrm{dc}}}{\pi}, U_{\mathrm{ac}(i)}=\frac{2\sqrt{2}U_{\mathrm{dc}(i)}}{\pi}(i=1,2). \tag{1}$$

When the pickups receive power, the ac equivalent impedance in each pickup can be given by $R_{l(i)}=8R_i/\pi^2$ $(i=1,2)$.

A. Operation Mode 1(Normal Mode)

Fig. 3 shows the equivalent circuit of operation mode 1. In this mode, the track coil provides energy for multiple pickups. L_T–C_T series resonant topology is adopted in the track side. The energy in the track is injected by a primary power source with the aid of a full-bridge inverter and an *LCL* resonant network. Compared with the conventional track WPT system, the proposed track resonant system is designed independent of its power-driving stage. This design is helpful for operation under multiple-power-source injection mode.

According to the equivalent circuit of the operation mode 1 in Fig. 3, the total impedance of each pickup $Z_{s(i)}$ can be given by

$$\begin{aligned}Z_{s(i)}&=j\omega L_{s(i)}+\left(R_{l(i)}+j\omega L_{so(i)}\right)//\frac{1}{j\omega C_{s(i)}}\\&=\frac{\begin{array}{l}j\omega\left(L_{s(i)}+L_{so(i)}-\omega^2L_{s(i)}L_{so(i)}C_{s(i)}\right)\\+R_{l(i)}\left(1-\omega^2C_{s(i)}L_{so(i)}\right)\end{array}}{1-\omega^2C_{s(i)}L_{s(i)}+j\omega C_{s(i)}R_{l(i)}}\end{aligned}^{(i=1,2)}. \tag{2}$$

If $L_{s(i)}$, $L_{so(i)}$, and $C_{s(i)}$ satisfy (3), $Z_{s(i)}$ can be expressed as (4)

$$\omega^2=\frac{1}{L_{s(i)}C_{s(i)}}=\frac{1}{L_{so(i)}C_{s(i)}}\,(i=1,2) \tag{3}$$

$$Z_{s(i)}=\frac{\omega^2L_{so(i)}^2}{R_{l(i)}}\,(i=1,2)\,. \tag{4}$$

The total impedance of the track Z_t can be given by

$$\begin{aligned}Z_t&=j\omega L_T+\frac{1}{j\omega C_T}+\sum_{i=1}^{2}\frac{(\omega M_i)^2}{Z_{s(i)}}=j\omega L_T+\frac{1}{j\omega C_T}\\&\quad+\sum_{i=1}^{2}\frac{M_i^2R_{l(i)}}{L_{so(i)}^2}.\end{aligned} \tag{5}$$

If L_T and C_T satisfy (6), Z_t can be expressed as (7)

$$\omega^2=\frac{1}{L_TC_T} \tag{6}$$

$$Z_t=\sum_{i=1}^{2}\frac{M_i^2R_{l(i)}}{L_{so(i)}^2}. \tag{7}$$

The reflected impedance in the primary coil from the track Z_p can be given by

$$Z_p=\frac{(\omega M)^2}{Z_t}=\frac{(\omega M)^2}{\sum_{i=1}^{2}\frac{M_i^2R_{l(i)}}{L_{so(i)}^2}}. \tag{8}$$

The total impedance of the primary Z can be given by

$$\begin{aligned}Z&=j\omega L_{pi}+(Z_p+j\omega L_p)//\frac{1}{j\omega C_p}\\&=\frac{j\omega\left(L_{pi}+L_p-\omega^2L_{pi}L_pC_p\right)+Z_p\left(1-\omega^2C_pL_p\right)}{1-\omega^2C_pL_{pi}+j\omega C_pZ_p}\end{aligned} \tag{9}$$

If L_p, L_{pi}, and C_p satisfy (10), Z can be expressed as (11)

$$\omega^2=\frac{1}{L_{pi}C_p}=\frac{1}{L_pC_p} \tag{10}$$

$$Z=\frac{\omega^2L_p^2}{Z_p}=\frac{L_p^2\sum_{i=1}^{2}\frac{M_i^2R_{l(i)}}{L_{so(i)}^2}}{M^2}. \tag{11}$$

According to (4), (7), and (11), under the condition of (3), (6), and (10), the equivalent impedances of *LCL* and SS resonant network exhibit resistive characteristic, and the resonance frequency is independent of the loads and the mutual inductances.

In the operation mode 1, the KVL equation of the primary side can be given by

$$\begin{cases}\dot{U}_{ac}=\left(j\omega L_{pi}+\frac{1}{j\omega C_p}\right)\dot{I}_{Lpi}-\frac{1}{j\omega C_p}\dot{I}_p\\0=-\frac{1}{j\omega C_p}\dot{I}_{Lpi}+\left(j\omega L_p+\frac{1}{j\omega C_p}+Z_p\right)\dot{I}_p.\end{cases} \tag{12}$$

According to (10), the current in the primary coil can be given by

$$\dot{I}_p=-\dot{U}_{ac}j\omega C_p=-j\frac{\dot{U}_{ac}}{\omega L_p}. \tag{13}$$

The track current can be obtained by

$$\dot{I}_t=\frac{j\omega M\dot{I}_p}{Z_t}=\frac{\dot{U}_{\mathrm{ac}}M}{L_p\left(\sum_{i=1}^{2}\frac{M_i^2R_{l(i)}}{L_{so(i)}^2}\right)}. \tag{14}$$

The current in the pickup inductance $L_{so(i)}$ can be given by

$$\dot{I}_{so(i)}=\frac{\dot{U}_{ac}MM_i}{L_pL_{so(i)}\left(\sum_{i=1}^{2}\frac{M_i^2R_{l(i)}}{L_{so(i)}^2}\right)}\,(i=1,2)\,. \tag{15}$$

This current is also the current in the load, and the output voltage can be given by

$$\dot{U}_{o(i)}=\frac{\dot{U}_{ac}MM_iR_{l(i)}}{L_pL_{so(i)}\left(\sum_{i=1}^{2}\frac{M_i^2R_{l(i)}}{L_{so(i)}^2}\right)}\,(i=1,2)\,. \tag{16}$$

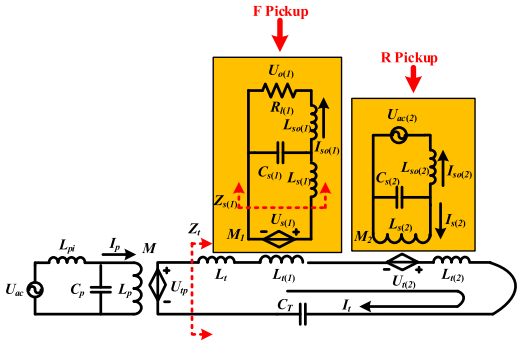

Fig. 4. Equivalent circuit of operation mode 2.

The output power of each pickup can be given by

$$P_{o(i)} = \left(\frac{U_{ac} M M_i}{L_p L_{so(i)} \left(\sum_{i=1}^{2} \frac{M_i^2 R_{l(i)}}{L_{so(i)}^2} \right)} \right)^2 R_{l(i)} \, (i = 1, 2) \, . \tag{17}$$

B. Operation Mode 2 (Strengthening Mode)

Operation mode 2 is designed for strengthening the energy transfer capability. In this condition, one pickup requires higher power than the rating power in a short interval. The normal mode cannot meet the transient sharp power requirement. The operation mode 2 provides an energy injection channel from other pickups to the track.

Fig. 4 shows the equivalent circuit of operation mode 2. In this mode, the induced voltage of the track coil can be divided into two parts: one part is from the primary coil coupling, and the other part is from the reverse injection pickup (R pickup) coil coupling. When the pickup reversely injects energy, the current in the R pickup coil is given by

$$\dot{I}_{s(2)} = -j \frac{\dot{U}_{ac(2)}}{\omega L_{s(2)}} . \tag{18}$$

The current in the track can be obtained by

$$\begin{aligned} \dot{I}_t &= \frac{1}{Z_t} \left(\frac{\dot{U}_{\mathrm{ac}} M}{L_p} + \frac{\dot{U}_{\mathrm{ac}(2)} M_2}{L_{s(2)}} \right) \\ &= \frac{\dot{U}_{\mathrm{ac}} M L_{so(1)}^2}{L_p M_1^2 R_{l(1)}} + \frac{\dot{U}_{\mathrm{ac}(2)} M_2 L_{so(1)}^2}{L_{s(2)} M_1^2 R_{l(1)}} . \end{aligned} \tag{19}$$

The current in the forward receiving pickup (F pickup) inductance $L_{so(1)}$ is given by

$$\dot{I}_{so(1)} = \frac{\dot{U}_{ac} M L_{so(1)}}{L_p M_1 R_{l(1)}} + \frac{\dot{U}_{ac(2)} M_2 L_{so(1)}}{L_{s(2)} M_1 R_{l(1)}} = A + B \tag{20}$$

where

$$\begin{cases} A = \frac{\dot{U}_{\mathrm{ac}} M L_{so(1)}}{L_p M_1 R_{l(1)}} \\ B = \frac{\dot{U}_{\mathrm{ac}(2)} M_2 L_{so(1)}}{L_{s(2)} M_1 R_{l(1)}} . \end{cases} \tag{21}$$

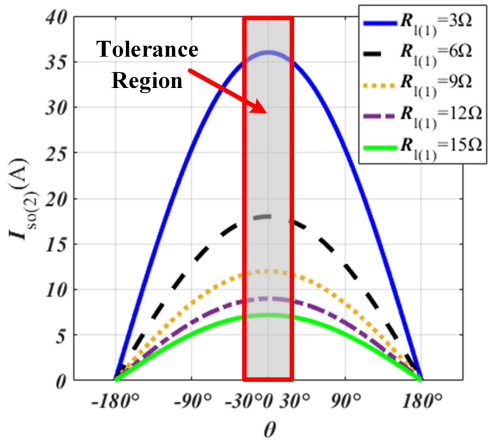

Fig. 5. Relationship between $I_{so(2)}$ and θ.

III. Synchronization

In the energy strengthening mode, at least two high-frequency sources (primary and R pickup) inject energy to the track. It is necessary to synchronize the ac phase between the multiple power sources. In this section, a synchronization method is applied to eliminate the risk of magnetic field cancelation between multiple energy injection sides, and it can eliminate communication equipment among the primary and multiple pickups.

In the operation mode 1, only the primary source provides energy for the track resonant system. If only one pickup obtains energy from the track, the output voltage of the pickup can be given by

$$\dot{U}_{o(1)} = A R_{l(1)} . \tag{22}$$

In the operation mode 2, the primary and the R pickup will provide energy for the F pickup. The output voltage of the F pickup can be given by

$$\dot{U}_{o(1)} = (A + B) \, R_{l(1)} \tag{23}$$

where the definition of A and B is given in (20). It can be seen from (22) and (23) that, if the phase between A and B is mismatched, the output voltage of the F pickup will decrease. As a result, the reverse energy injection will be blocked and the power transfer capability will be reduced. Therefore, a method is proposed to synchronize the phase between A and B. The control strategy can be shown as follows.

In the operation mode 2, the current in the $L_{so(2)}$ of the R pickup can be given by

$$\begin{aligned} \dot{I}_{so(2)} = \frac{M_2 L_{s(1)}^2}{L_{s(2)} M_1^2 R_{l(1)}} \left(\left(\frac{|U_{ac}| \, M}{L_p} + \frac{|U_{ac(2)}| \, M_2}{L_{s(2)}} \cos\theta \right) \right. \\ \left. + \, j \frac{|U_{ac(2)}| \, M_2}{L_{s(2)}} \sin\theta \right) \end{aligned} \tag{24}$$

where θ is the relative phase angle between U_{ac} and $U_{\mathrm{ac}(2)}$.

From (24) and Fig. 5, it can be inferred that when θ varies from –180° to 180°, $I_{so(2)}$ undergoes a corresponding variation

from 0 to its peak value and returns to 0. The current $I_{so(2)}$ approaches its peak value when θ approaches 0, which indicates that $U_{\rm ac}$ and $U_{\rm ac(2)}$ are in phase and *A* and *B* are synchronized. Therefore, the peak value of $I_{so(2)}$ can be utilized to evaluate the synchronization state of *A* and *B*. When *A* and *B* are not synchronized, we can adjust the phase of the R pickup to maintain $U_{\rm ac}$ and $U_{\rm ac(2)}$ in phase. However, in the application, the track process is sensitive to external interference only if the peak point is set as the track objective. A tolerance region should be set to reduce the sensitivity in the tracking. The tolerance region is defined as a small region around $\theta = 0$.

The influence of the voltage ripple defines the reference of the tolerance region. $I_{so(2)}$ is detected by current hall sensor and then rectified and filtered. However, in the implementation, the voltage ripple is 3% after filtering, so in order to improve the stability of the system, 97% peak value of $I_{so(2)}$ should be set as a reference. According to (24), The root mean square (rms) of $I_{so([2)}$ is

$$I_{so(2)} = \frac{M_2 L_{s(1)}^2}{L_{s(2)} M_1^2 R_{l(1)}} \times \sqrt{\left(\frac{|U_{\rm ac}|\, M}{L_p} + \frac{|U_{\rm ac(2)}|\, M_2}{L_{s(2)}} \cos\theta\right)^2 + \left(\frac{|U_{\rm ac(2)}|\, M_2}{L_{s(2)}} \sin\theta\right)^2}. \tag{25}$$

The current $I_{so(2)}$ approaches its peak value when θ approaches 0, which indicates that $U_{\rm ac}$ and $U_{\rm ac(2)}$ are in phase. When θ approaches 0, the rms of $I_{so(2)}$ is

$$I_{so(2)} = \frac{M_2 L_{s(1)}^2}{L_{s(2)} M_1^2 R_{l(1)}} \left(\frac{|U_{\rm ac}|\, M}{L_p} + \frac{|U_{\rm ac(2)}|\, M_2}{L_{s(2)}}\right). \tag{26}$$

When phase θ approaches 30°, the rms of $I_{so(2)}$ is as (27), shown at the bottom of this page.

Under the condition of experimental system, the ratio between $I_{so(2)}(30°)$ ($\theta = 30°$) and $I_{so(2)}(0)$ ($\theta = 0$) is as (28), shown at the bottom of this page.

The ratio between $I_{so(2)}(\theta)$ and $I_{so(2)}(0)$ is shown in Fig. 6. According to the above analysis, when the tolerance region is selected as ±30°, 97% peak value of $I_{so(2)}$ is achieved and the influence of the 3% ripple voltage is ignored, then the system stability is improved.

The flowchart of the synchronization controller is illustrated in Fig. 7. First, the same frequency is selected to drive S_{p1}–S_{p4} and S_{11}–S_{14}. The initial phase-shift angle of S_{11}–S_{14} is φ. The resonant current $I_{so(2)}$ is detected to determine whether it is entering the tolerance region. If the tolerance region is reached, the phase-shift angle is selected to drive S_{11}–S_{14}. Otherwise, it will continue to increase the phase angle to reach the tolerance region. The synchronization method shown in Fig. 7 is only a single loop. In the implementation, $I_{so(2)}$ is detected continually. If the phase restarts drifting, the system will repeat adjusting the phase of the R pickup until $U_{\rm ac}$ and $U_{\rm ac(2)}$ are in phase.

In the synchronization method, to obtain a high response speed, a special current track circuit is designed and implemented. Fig. 8 presents the schematic of this circuit.

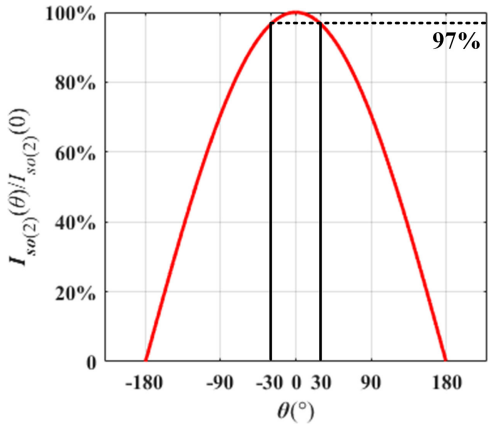

Fig. 6. Ratio between $I_{so(2)}(\theta)$ and $I_{so(2)}(0)$.

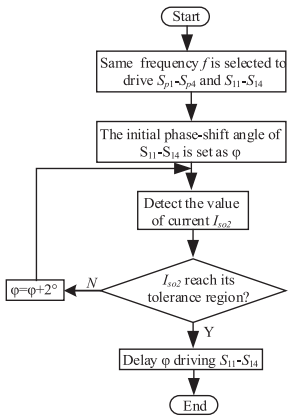

Fig. 7. Method of synchronization.

$$I_{so(2)} = \frac{M_2 L_{s(1)}^2}{L_{s(2)} M_1^2 R_{l(1)}} \sqrt{\left(\frac{|U_{\rm ac}|\, M}{L_p} + \frac{|U_{\rm ac(2)}|\, M_2}{L_{s(2)}} \cos 30°\right)^2 + \left(\frac{|U_{\rm ac(2)}|\, M_2}{L_{s(2)}} \sin 30°\right)^2} \tag{27}$$

$$\frac{I_{so(2)}\,(30°)}{I_{so(2)}\,(0)} = \frac{\sqrt{\left(\frac{|U_{\rm ac}|M}{L_p} + \frac{|U_{\rm ac(2)}|M_2}{L_{s(2)}} \cos 30°\right)^2 + \left(\frac{|U_{\rm ac(2)}|M_2}{L_{s(2)}} \sin 30°\right)^2}}{\frac{|U_{\rm ac}|M}{L_p} + \frac{|U_{\rm ac(2)}|M_2}{L_{s(2)}}} \approx 97\% \tag{28}$$

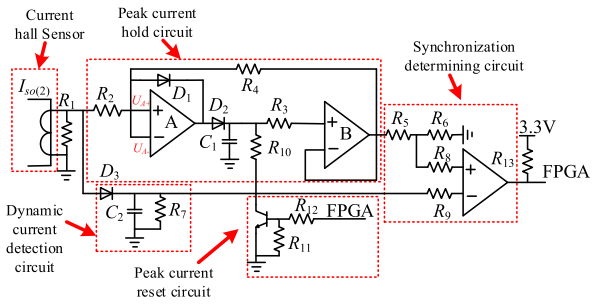

Fig. 8. Current track circuit.

As can be seen in Fig. 8, there are five parts in the synchronization circuit: current hall sensor, peak current hold circuit, dynamic current detection circuit, synchronization determining circuit, and peak current reset circuit.

The principle of the synchronization circuit is explained as follows. According to the above analysis, the synchronization status is determined by whether $I_{so(2)}$ reaches its peak value.

1) Synchronized: $I_{so(2)}$ reaches its peak value.
2) Not synchronized: $I_{so(2)}$ is lower than its peak value, and the inverter phase of the R pickup should be adjusted to make the current reach the peak value.

To realize the above objective, a peak current hold circuit is designed by using two operational amplifiers, including A and B, to track the peak current and hold it. To reduce the influence of disturbance, a tolerance region is set around the peak value. To make the synchronization circuit adaptive for load and mutual inductance variation, a reset circuit is used to reset the peak current. Every part of the synchronization circuit can be given as follows.

1) Current hall sensor: A current hall sensor is utilized to detect current $I_{so(2)}$ in the inductance $L_{so(2)}$ of the R pickup.
2) Peak current hold circuit: A peak current hold circuit is utilized to obtain and maintain the peak value of $I_{so(2)}$. The operational amplifier A is utilized to track the peak current and the operational amplifier B works as a voltage follower to hold it.
3) Dynamic current detection circuit: The dynamic current $I_{so(2)}$ is rectified by D_3 and filtered by C_2.
4) Synchronization determining circuit: A comparator will detect whether the current $I_{so(2)}$ reaches its peak value, and the field-programmable gate array (FPGA) controller will adjust the inverter phase of the R pickup to approach its peak value via a status signal. On this basis, R_5 and R_6 set a tolerance region to reduce the influence of disturbance.
5) Peak current reset circuit: If the F pickup needs to track lower power level, the FPGA chip makes the peak current hold circuit reset, and then $I_{so(2)}$ tracks the low power level.

When A and B are synchronized, the output power of the F pickup can be obtained by

$$P_{o(i)} = |A + B|^2 R_{l(1)}. \tag{29}$$

As seen from (22) and (29), compared with operation mode 1, operation mode 2 provides higher power.

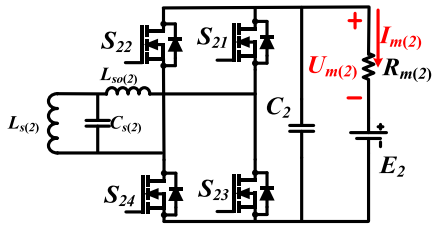

Fig. 9. Equivalent circuit diagram of R pickup in operation mode 2.

IV. Boundary Condition of Reverse Energy Injection

Fig. 9 depicts the equivalent circuit diagram of the R pickup in operation mode 2. The boundary condition gives a limitation for reverse energy injection. In the strengthening mode, if input voltage of the R pickup is not large enough, it will block energy reverse injection process and make R pickup work as a receiver. The boundary condition gives a minimum input voltage of R pickup. The battery of the R pickup can be expressed as a series connection of voltage source E_2 and resistance $R_{m(2)}$. Applying superposition theorem, $U_{m(2)}$ can be expressed as follows:

$$U_{m(2)} = \frac{\pi U_{\rm ac} M M_2 R_{m(2)}}{2\sqrt{2} L_p L_{so(2)} \left(\frac{M_1^2 R_{l(1)}}{L_{so(1)}^2} + \frac{M_2^2 R_{m(2)}}{L_{so(2)}^2} \right)} - E_2. \tag{30}$$

Then, the current $I_{m(2)}$ can be expressed as follows:

$$I_{m(2)} = \frac{U_{m(2)}}{R_{m(2)}}. \tag{31}$$

The energy $P_{E(2)}$ received or delivered on battery E_2 can be expressed as

$$P_{E(2)} = E_2 I_{m(2)}. \tag{32}$$

Equations (30)–(32) show that when $U_{m(2)} > 0$ and $P_{E(2)} > 0$, the battery receives energy; when $U_{m(2)} < 0$ and $P_{E(2)} < 0$, the battery delivers energy for other pickups. Therefore, we must satisfy $U_{m(2)} < 0$ to make the energy transfer reversely. Usually, when the battery is used as a power source, its resistance $R_{m(2)}$ is relatively small. According to (30), when $R_{m(2)}$ is relatively small, generally $U_{m(2)} < 0$. Therefore, the energy can be easily reversely transferred.

When the system works in operation mode 2, F pickup receives energy from the primary and the R pickup. Equation (33) indicates that the energy is inversely injected from the R pickup to the F pickup. Under such condition, the energy P_{FB} transferred by the R pickup can be obtained as follows:

$$P_{FB} = \frac{U_{\rm ac(2)} M_2}{L_{s(2)}} \left(\frac{U_{\rm ac} M L_{so(1)}^2}{L_p M_1^2 R_{l(1)}} + \frac{U_{\rm ac(2)} M_2 L_{so(1)}^2}{L_{s(2)} M_1^2 R_{l(1)}} \right). \tag{33}$$

V. Performance Analysis

As mutual inductances and equivalent resistances dynamically change during the moving charging process, it is necessary to analyze and evaluate the effects of these variations on the system performance under the two operation modes. The output

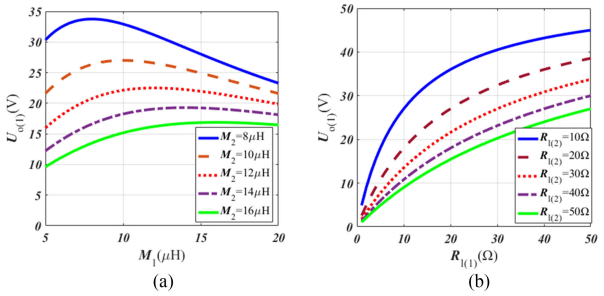

Fig. 10. Variation of $U_{o(1)}$ with the mutual inductances and the loads in operation mode 1. (a) Variation of $U_{o(1)}$ with mutual inductances. (b) Variation of $U_{o(1)}$ with load resistances.

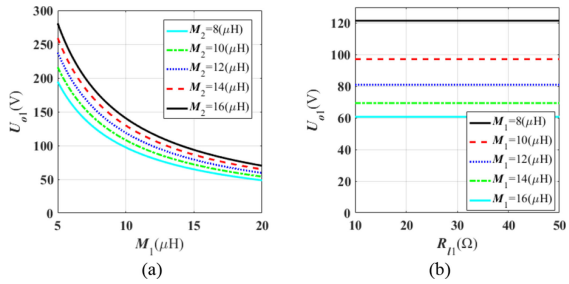

Fig. 11. Variation of $U_{o(1)}$ with the mutual inductances and the load in operation mode 2. (a) Variation of $U_{o(1)}$ with M_1 and M_2. (b) Variation of $U_{o(1)}$ with M_1 and R_{l1}.

voltage on the load in mode 1 can be obtained as follows:

$$\dot{U}_{o(1)} = \frac{\dot{U}_{\mathrm{ac}} M M_1 R_{l(1)}}{L_p L_{so(1)} \left(\sum_{i=1}^{2} \frac{M_i^2 R_{l(i)}}{L_{so(i)}^2} \right)}. \tag{34}$$

Through the theoretical analysis, Fig. 10 shows the variation of the output voltage $U_{o(1)}$ with the mutual inductances and the loads. It can be seen from Fig. 10(a) that, $U_{o(1)}$ undergoes a raising and falling process with the increase of M_1, and a falling process with the increase of M_2. From Fig. 10(b), it can be seen that $U_{o(1)}$ increases with the increase of $R_{l(1)}$ and decreases with the increase of $R_{l(2)}$.

When the system works in mode 1 with only one pickup, the output voltage on the load can be expressed as follows:

$$\dot{U}_{o(1)} = \frac{\dot{U}_{\mathrm{ac}} L_{so(1)} M}{L_p M_1}. \tag{35}$$

When the system works in mode 2, the output voltage of the F pickup can be expressed as follows:

$$\dot{U}_{o(1)} = \frac{L_{so(1)}}{M_1} \left(\frac{\dot{U}_{\mathrm{ac}} M}{L_p} + \frac{\dot{U}_{\mathrm{ac}(2)} M_2}{L_{s(2)}} \right). \tag{36}$$

Through the theoretical analysis, the variation of $U_{o(1)}$ with the mutual inductances and the load in operation mode 2 is shown in Fig. 11. As can be seen from Fig. 11(a), $U_{o(1)}$ decreases with the increase of M_1 and increases with the increase of M_2, the maximum of U_{o1} is 270 V when $M_1 = 5$ μH, $M_2 = 16$ μH, and the minimum of U_{o1} is 50 V when $M_1 = 20$ μH and $M_2 = 8$ μH. As can be seen from Fig. 11(b), U_{o1} is independent of the load.

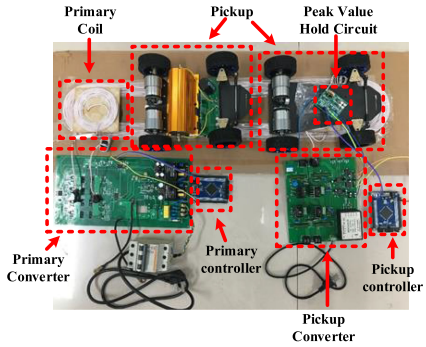

Fig. 12. Experimental setup.

TABLE I
PARAMETERS OF THE TRACK WPT SYSTEM

Parameters	Value	Parameters	Value
U_{dc}	35 V	L_{pi}	35.3 μH
L_p	35.2 μH	C_p	32 nF
R_p	0.139 Ω	M	10.15 μH
L_T	57.32 μH	C_t	19.64 nF
R_t	0.132 Ω	$L_{s(1)}$	33.2 μH
$L_{so(1)}$	33.19 μH	$C_{s(1)}$	33.92 nF
$R_{s(1)}$	0.09 Ω	M_1	12.675 μH
$L_{s(2)}$	25.2 μH	$C_{s(2)}$	44.5 nF
$L_{so(2)}$	25 μH	$R_{s(2)}$	0.05 Ω
M_2	9.675 μH	$U_{dc(2)}$	35 V
R_1	8 Ω	R_2	8 Ω
F	150 kHz		

VI. EXPERIMENTAL VERIFICATION

In order to verify the proposed method, an experimental system is set up as shown in Fig. 12, which wirelessly charges for two moving robots. FPGA chip (EP2C5T144C8) is selected as the main control unit and MOSFET SiHG32N50D as the main switching component. The experimental system consists of one primary side, one track unit, and two pickups. The primary coil and the pickup coils are circular coils with 100 mm diameter and the track coil is an 800 mm straight coil. The air gap between primary side and track is 30 mm, which is the same as the distance between the pickups and track.

In the resonant topology design, an *LCL* topology is selected for the primary and pickups, and a series *LC* topology is selected for the track unit. In the mode 1 test, the primary with 35 V dc input voltage provides energy for the track and the two pickup loads with 8 Ω resistance.

In the mode 2 test, the dc input voltage of the primary and the R pickup are both 35 V, and they provide energy for the F pickup with 8 Ω resistance. The current track circuit is utilized in the R pickup for synchronization between the R pickup and the primary. The driving signals of the inverters in the primary and R pickup are given by the FPGA controller, and the system parameters are tabulated in Table I.

To verify the proposed method, three kinds of tests can be carried out as follows:

1) operation test in mode 1 with two pickups receiving energy;
2) operation test in mode 1 with one pickup receiving energy;
3) operation test in mode 2.

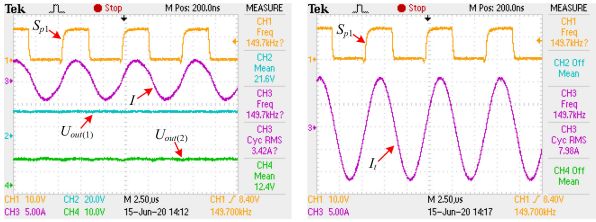

Fig. 13. Operation model 1 with two pickups. (a) Driving signal of MOSFET S_{p1}, current in the primary inductance L_{pi} and output voltage in two pickups. (b) Driving signal of MOSFET S_{p1} and current in the track.

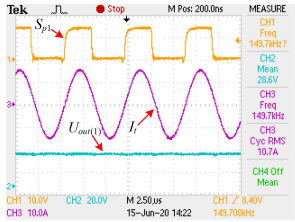

Fig. 14. Operation model 1 with one pickup.

A. Operation Mode 1 With Two Pickups

Fig. 13 shows experimental waveforms in the operation mode 1 with two pickups. Fig. 13(a) shows the driving signal of MOSFET S_{p1}, the current in the primary inductance L_{pi}, and the output voltage of two pickups. Fig. 13(b) shows the driving signal of MOSFET S_{p1} and the current in the track. As can be seen from the two figures, $U_{\mathrm{out}(1)} = 21.6$ V, $U_{\mathrm{out}(2)} = 12.4$ V, $I_t = 7.98$ A, and then it is calculated that $P_{\mathrm{out}(1)} = 58.32$ W and $P_{\mathrm{out}(2)} = 19.22$ W.

B. Operation Mode 1 With One Pickup

According to (14) and (16), when there are fewer pickups in the operation mode 1, it provides more current for the track and higher power for the pickups. Fig. 14 shows the driving signal of S_{p1}, the current in the track, and the output voltage on the load in the operation mode 1 with one pickup. It can be observed that, compared with Fig. 13(a), the output voltage on the load increases from 21.6 to 28.6 V and the output power increases from 58.32 to 102.25 W in Fig. 14. Simultaneously, compared with Fig. 13(b), the current in the track increases from 7.98 to 10.7 A. It is known that the experimental results are all consistent with the theoretical results.

C. Operation Mode 2

The experimental results of the operation mode 2 are shown in Fig. 15. Fig. 15(a) and (b) show the driving signals of S_{p1} and S_{21}, the current $I_{so(2)}$ in inductance $L_{so(2)}$, and the output voltage $U_{\mathrm{out}(1)}$ when U_{ac} and $U_{\mathrm{ac}(2)}$ are in phase or not in phase. Fig. 15(c) shows the driving signal of S_{p1} and S_{21}, and the current in the track when U_{ac} and $U_{\mathrm{ac}(2)}$ are in phase. By comparing Fig. 15(a) with (b), it can be seen that when the driving signals of S_{p1} and S_{21} are not in phase, both the output voltage $U_{\mathrm{out}(1)}$ of the F pickup and the current $I_{so(2)}$ in the R pickup decrease, which is consistent with the theoretical result. It

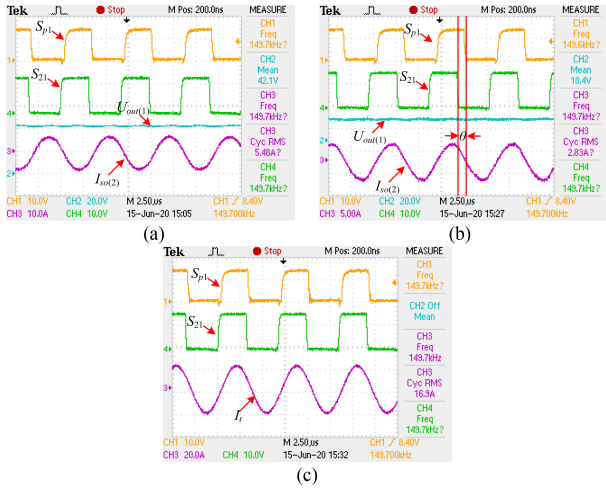

Fig. 15. Operation mode 2. (a) U_{ac} and $U_{\mathrm{ac}(2)}$ are in phase. (b) U_{ac} and $U_{\mathrm{ac}(2)}$ are not in phase. (c) U_{ac} and $U_{\mathrm{ac}(2)}$ are in phase.

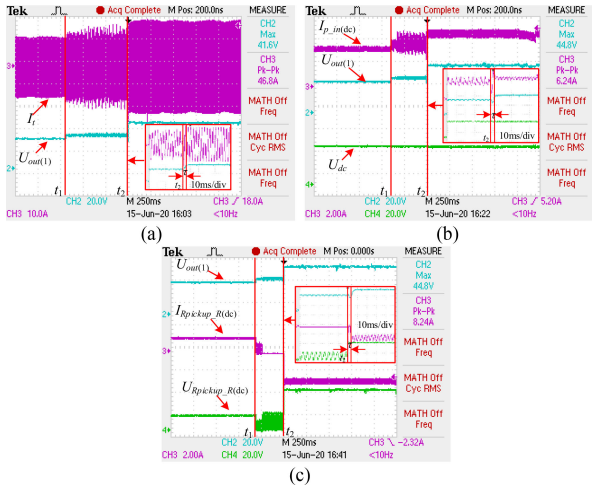

Fig. 16. Dynamic regulation process of the system. (a) Variation of the output voltage $U_{\mathrm{out}(1)}$ and track current I_t. (b) Variation of the input current $I_{p\_\mathrm{in(dc)}}$, the input voltage U_{dc} in the primary side, and $U_{\mathrm{out}(1)}$. (c) Variation of the voltage $U_{R\mathrm{pickup\_}R(\mathrm{dc})}$, the current $I_{R\mathrm{pickup\_}R(\mathrm{dc})}$ in the R pickup side, and $U_{\mathrm{out}(1)}$.

can be observed from Figs. 14 and 15(c) that the track current in operation mode 2 increases from 10.7 to 16.9 A when compared with that in operation mode 1. Also, it can be observed in Figs. 14 and 15(a) that when U_{ac} and $U_{\mathrm{ac}(2)}$ are in phase, the output voltage increases from 28.6 to 42.1 V and the output power of the F pickup increases from 102.25 to 221.55 W. This verifies that the power transfer capability is strengthened after R pickup reversely injects energy.

D. Dynamic Regulation Process of the System

The dynamic adjustment process of the system when it changes from operation mode 1 to operation mode 2 is shown in Fig. 16. Fig. 16(a) shows the output voltage $U_{\mathrm{out}(1)}$ of the F pickup and track current I_t during the switching process of the operation modes and phase-shifting regulation. Fig. 16(b) shows the input current $I_{p\_\mathrm{in(dc)}}$, the input voltage U_{dc} of the primary, and $U_{\mathrm{out}(1)}$. Fig. 16(c) shows the voltage $U_{R\mathrm{pickup\_}R(\mathrm{dc})}$, the

current $I_{R\text{pickup}\_R(\text{dc})}$ of the R pickup, and $U_{\text{out}(1)}$. In the experimental system, the load of the R pickup consists of a resistance and a dc power source connected in parallel. The ON/OFF of the two branches is controlled via switches.

When $t < t_1$, the resistance branch of the R pickup is "ON" while the power source branch is "OFF," and the system works in the operation mode 1, in which the converter of the R pickup works as a rectifier, and the R pickup receives energy.

When $t = t_1$, the converter of the R pickup changes from rectifier to inverter, the operating frequency of the inverter is the same as that of the primary, and the resistance branch is OFF. During this time, the primary and R pickup inverters are not synchronized. The resistance branch may be short-circuited due to the different phase of the primary and R pickup inverters. The reflected impedance from the R pickup to the track coil will decrease. This causes the track current and the voltage received by the F pickup to increase. Furthermore, the input power increases as the output power increases. Thus, the primary current increases. Therefore, from Fig. 16, it can be seen that I_t, $I_{p\_\text{in}(\text{dc})}$ and $U_{\text{out}(1)}$ increase slightly.

When $t = t_2$, the power branch is ON, and the controller in the R pickup maintains U_{ac} and $U_{\text{ac}(2)}$ in the same phase via phase-shifting adjustment with an adjustment time τ. After that, the system works in operation mode 2. It can be seen from Fig. 16 that I_t, $I_{p\_\text{in}(\text{dc})}$ and $U_{\text{out}(1)}$ increase significantly, the input current of the R pickup is reversed, and the R pickup changes from receiving energy to transmitting energy. The phase of U_{ac} and $U_{\text{ac}(2)}$ can be adjusted to the same less than 1 ms. Meanwhile, the switching process is stable, and large voltage and current spikes do not occur in any part of the system.

When the system operates in mode 1 with one pickup, the output voltage of the pickup can be given by

$$U_{\text{out}(1\_1)} = \frac{\pi U_{\text{ac}} M L_{so(1)}}{2\sqrt{2} L_p M_1} = 28.6\text{V}. \tag{37}$$

When the system operates in mode 2, the output voltage of the F pickup can be given by

$$\begin{aligned} U_{\text{out}(1)(2)} &= \frac{\pi U_{\text{ac}} M L_{so(1)}}{2\sqrt{2} L_p M_1} + \frac{\pi U_{\text{ac}(2)} M_2 L_{so(1)}}{2\sqrt{2} L_{s(2)} M_1} \\ &= U_{\text{out}(1\_1)} + U_{\text{out}(1\_2)} = 42.1\text{V}. \end{aligned} \tag{38}$$

When the system operates in mode 2, the power received by the F pickup can be given by

$$\begin{aligned} P_{\text{out}(1)} &= \frac{U^2_{\text{out}(1)(2)}}{R_1} = \frac{1}{R_1}\left(U_{\text{out}(1\_1)} + U_{\text{out}(1\_2)}\right)^2 \\ &= 221.55\text{W}. \end{aligned} \tag{39}$$

The reverse energy provided by the R pickup to the F pickup can be given by

$$\begin{aligned} P_{\text{out}(1)(R\text{Pickup})} &= \frac{1}{R_1}\left(U^2_{\text{out}(1\_2)} + U_{\text{out}(1\_1)} U_{\text{out}(1\_2)}\right) \\ &= 71.04\text{W}. \end{aligned} \tag{40}$$

TABLE II
COMPARISON OF EXPERIMENTAL RESULT

	$U_{out(1)}$ (V)	$U_{out(2)}$ (V)	$P_{out(1)}$ (W)	$P_{out(1)}$ (*primary*) (W)	$P_{out(1)}$ (*R pickup*) (W)	$P_{out(2)}$ (W)
Operation mode 1 with two pickups	21.6	12.4	58.32	58.32		19.2
Operation mode 1 with one pickup	28.6		102.25	102.25		
Operation mode 2 (U_{ac} and $U_{ac(2)}$ is in phase)	42.1		221.55	150.51	71.04	
Operation mode 2 (U_{ac} and $U_{ac(2)}$ is not in phase)	18.4		42.32			

TABLE III
VARIATION OF THE MUTUAL INDUCTANCE M_{i} WITH THE MOVING DISTANCE

	M_i (μH)		
x (cm) \ y (cm)	0	2.5	5
0	10.01	9.95	9.55
25	10.02	9.96	9.56
50	10.53	10.24	9.33

The power provided by primary to the F pickup can be given by

$$\begin{aligned} P_{\text{out}(1)(\text{primary})} &= \frac{1}{R_1}\left(U^2_{\text{out}(1\_1)} + U_{\text{out}(1\_1)} U_{\text{out}(1\_2)}\right) \\ &= 150.51\text{W}. \end{aligned} \tag{41}$$

Table II gives the comparison results between mode 1 and mode 2.

As can be seen in Table II, compared to the operation mode 1, on the condition that U_{ac} and $U_{\text{ac}(2)}$ are in phase, the power transfer capability significantly increases via reverse energy injection of the R pickup. On the contrary, on the condition that U_{ac} and $U_{\text{ac}(2)}$ are not in phase, the output power of the F pickup decreases significantly. It can be seen that the synchronization plays an important role in the strengthening mode.

E. Variation Range of the Mutual Inductance During Motion, and the Influence of the Mutual Inductance Variation on the System Performance

This article focuses on the track application such as AGV moving along a stationary track. In this application, the relative movement between track and pickups is relatively small. Mutual inductance variation range is analyzed through COMSOL software. The COMSOL analysis model and magnetic field of the coupling mechanism are shown in Fig. 17.

In the COMSOL analysis model, the track coil is a 110 cm straight coil, and its width is 20 cm. The pickup coil is a circular coil with 10 cm diameter. The air gap between the track coil and the pickup coil is 3 cm. The starting position of the pickup coil movement is the center of the track coil. Within the range of coil movement shown in Table III, the variation of the mutual inductance M_i (i = 1, 2) between the two coils is shown in Fig. 18, and it is listed in Table III.

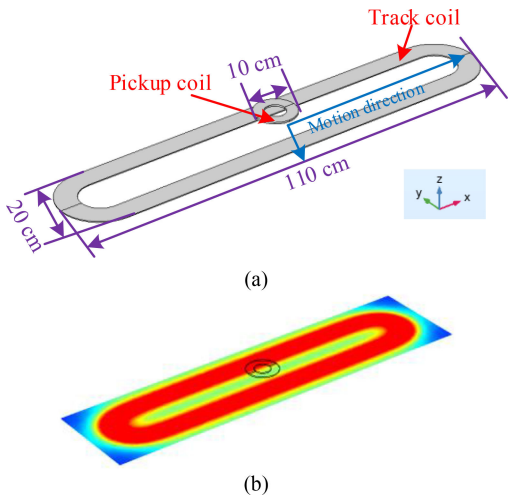

Fig. 17. COMSOL analysis model and magnetic field of the coupling mechanism. (a) COMSOL analysis model. (b) Magnetic field of the coupling mechanism.

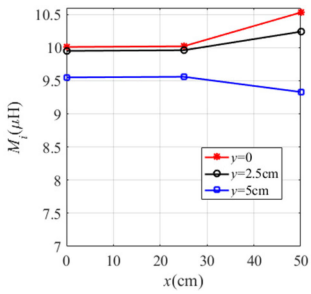

Fig. 18. Variation of the mutual inductance M_i with the moving distance.

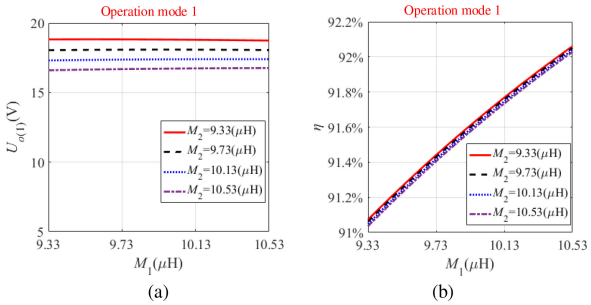

Fig. 19. Variations of the output voltage $U_{o(1)}$ and the efficiency η with the mutual inductance M_i in operation mode 1 (Normal mode). (a) Variation of $U_{o(1)}$ with M_i. (b) Variation of η with M_i.

Under the condition of the mutual inductance M_i variation shown in Fig. 18 and Table III, the influences of the M_i variation on the output voltage $U_{o(1)}$ and the efficiency η in two operation modes are shown as follows.

In operation mode 1, as can be seen from Fig. 19, when M_1 and M_2 vary from 9.33 to 10.53 μH, the output voltage $U_{o(1)}$ varies from 16.6 to 18.8 V, and the efficiency η varies from 91.12% to 92.05%. So $\Delta U_{o(1)} = 2.2$ V, $\Delta\eta = 0.93\%$. And the change ratio of $U_{o(1)}$ is 12%.

In operation mode 2, as can be seen from Fig. 20, when M_1 and M_2 increase from 9.33 to 10.53 μH, the output voltage $U_{o(1)}$ varies from 46.3 to 40.5 V, and the efficiency η varies from 91.9% to 93%. So $\Delta U_{o(1)} = 5.8$ V, $\Delta\eta = 1.1\%$. And the change ratio of $U_{o(1)}$ is 12.8%.

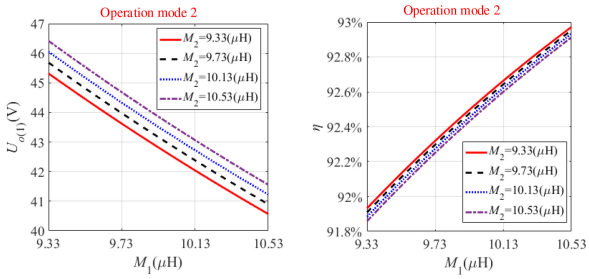

Fig. 20. Variations of the output voltage $U_{o(1)}$ and the efficiency η with the mutual inductance M_i in operation mode 2 (Strengthening mode). (a) Variation of $U_{o(1)}$ with M_i. (b) Variation of η with M_i.

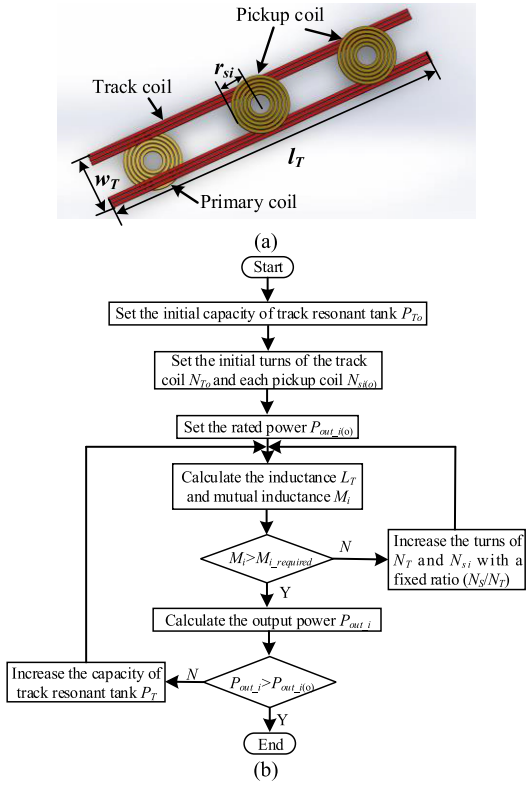

Fig. 21. Design method of track coil. (a) Typical track system structure. (b) Design steps of track system.

VII. Discussion

A. Design Method of Track System

Fig. 21(a) shows a typical track system structure. In the system designed in this article, the track resonant capacity plays an important role as it should meet the rated power requirement of each pickup with reduced costs.

The design steps of track system can be illustrated in Fig. 21(b). The track resonant capacity, turns of the track coil N_{To}, the pickup coil $N_{si(o)}$, and the rated power $P_{out\_i(o)}$ are initialized. Then, the inductance L_T can be calculated with (42). The mutual inductance M_i can be calculated with (43)–(45) and compared with $M_{i\_required}$. If M_i is higher than $M_{i\_required}$, the

output power $P_{\text{out\_}i}$ can be calculated. Or it will continue to increase the turns of N_T and N_{si} with a fixed ratio (N_S/N_T). If $P_{\text{out\_}i}$ is lower than $P_{\text{out\_}i(\text{o})}$, it will continue to increase the track resonant capacity P_T ($P_T = U_T I_T$, where U_T is the induced voltage of track coil), until it finally meets the rated power requirement

$$L_T = \frac{\mu_o N_T^2}{\pi}\left(w_T \ln\frac{l_T}{D_T/2} + l_T \ln\frac{w_T}{D_T/2}\right) \tag{42}$$

$$L_{si} = \mu_o r_{si} N_{si}^2\left(\ln\frac{8r_{si}}{D_{si}/2} - 2\right) \tag{43}$$

$$k_i = \frac{2r_{si}}{l_T}\left(\frac{r_{si}}{\sqrt{w_T^2 + 4h_i^2}}\right)^3 \tag{44}$$

$$M_i = k_i\sqrt{L_T L_{si}}. \tag{45}$$

μ_0 is the permeability constant. N_T, l_T, and w_T are the turns, length, and width of the track coil, respectively, and D_T is the wire diameter of the track coil. N_{si} and r_{si} are, respectively, the turns and the average radius of each pickup coil, and D_{si} is the wire diameter of each pickup coil. k_i and h_i are the coupling coefficient and height between the track coil and each pickup coil, respectively.

B. Future Application in EV Area

In dynamic wireless charging mode for EV, the ground excitation coils work as segment track coils. The proposed method can be utilized to increase track power capacity for the requirement of transient large power. It is especially useful for such a system with rapid power variation. However, there are several challenges in EV application as follows.

1) In the transient process from normal to strengthening mode, system resonance parameters should be designed carefully to avoid energy spike.
2) In EV dynamic charging, the switching of track coils will bring challenges to fast dynamic response of the controller in the strengthening mode.
3) In the track design of the proposed method, the dynamic EV wireless charging will cause dramatic mutual inductance and power variation. Seeking an optimum design for track resonance system is complicated. A multiple-objective design algorithm is needed to balance the system construction cost and power requirement.

C. Method is Generalized to More Than Two Sources

When there are n pickups in the system, the first pickup is assumed as F pickup to receive power, and the other pickups are as R pickups to inject power reversely.

The current in the inductance $L_{so(i)}$ of the R pickup can be given by

$$\dot{I}_{so(i)} = \frac{M_i L_{s(1)}^2}{L_{s(i)} M_1^2 R_{l(1)}}\left(\left(\frac{|U_{\text{ac}}|\,M}{L_p} + \sum_{i=2}^{n}\frac{|U_{\text{ac}(i)}|\,M_i}{L_{s(i)}}\cos\theta_i\right) + j\sum_{i=2}^{n}\frac{|U_{\text{ac}(i)}|\,M_i}{L_{s(i)}}\sin\theta_i\right)(i = 2, 3\ldots n) \tag{46}$$

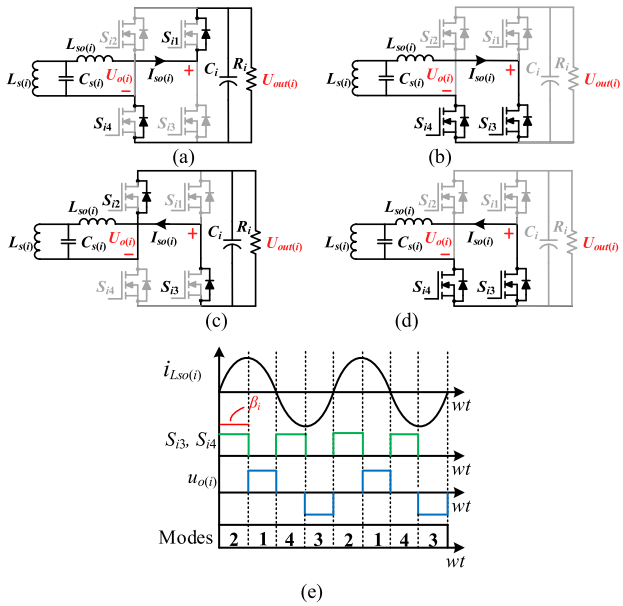

Fig. 22. Active rectifier and operating waveform. (a) Mode 1. (b) Mode 2. (c) Mode 3. (d) Mode 4. (e) Operating waveform.

where θ_i is the relative phase angle between U_{ac} and $U_{\text{ac}(i)}$. The current $I_{so(i)}$ approaches its peak value when θ_i approaches 0, which indicates that U_{ac} and $U_{\text{ac}(i)}$ are in phase. Therefore, the peak value of $I_{so(i)}$ can be utilized to evaluate the synchronization state of U_{ac} and $U_{\text{ac}(i)}$. When U_{ac} and $U_{\text{ac}(i)}$ are not synchronized, we can adjust the phase of the R pickup to make U_{ac} and $U_{\text{ac}(i)}$ in phase.

If there are multiple R pickups in the system, it is necessary to improve the response time of multiple R pickup controllers.

D. Output Voltage Regulation Through Active Rectifier

In the proposed system, a full-bridge converter is used in the pickup, so the converter can be used to adjust the output voltage. The analysis of the active-rectifier control method is as follows.

The active rectifier and operating waveform are shown in Fig. 22. There are four stages in one operating period, and the input voltage of the active rectifier $U_{o(i)}$ can be expressed as follows:

$$U_{o(i)} = \begin{cases} 0 & 0 < \omega t < \beta_i \\ U_{out(i)} & \beta_i < \omega t < \pi \\ 0 & \pi < \omega t < \pi + \beta_i \\ -U_{out(i)} & \pi + \beta_i < \omega t < 2\pi \end{cases} \tag{47}$$

where β_i is the conduction angle of the active rectifier and $U_{out(i)}$ is the output voltage. The rms value of $U_{o(i)}$ can be given by

$$U_{o(i)\_\text{rms}} = \frac{2\sqrt{2}}{\pi}U_{\text{out}(i)}\cos\frac{\beta_i}{2}.(0 < \beta_i < 180^\circ)\,(i = 1, 2)\,. \tag{48}$$

It can be seen from (48) that the output voltage can be adjusted by the conduction angle β_i. Its regulation ability on the output voltage $U_{\text{out}(1)}$ in two operation modes is shown in Fig. 23.

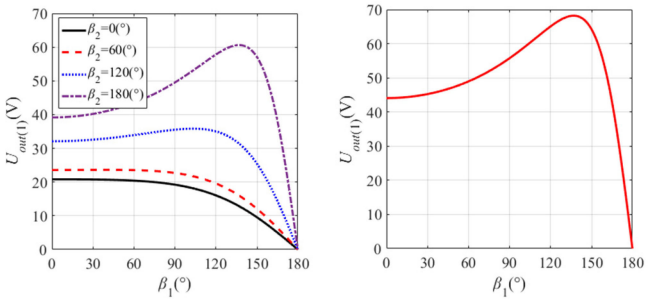

Fig. 23. Variation of the output voltage $U_{\mathrm{out}(1)}$ with β_i in two operation modes. (a) Operation mode 1. (b) Operation mode 2.

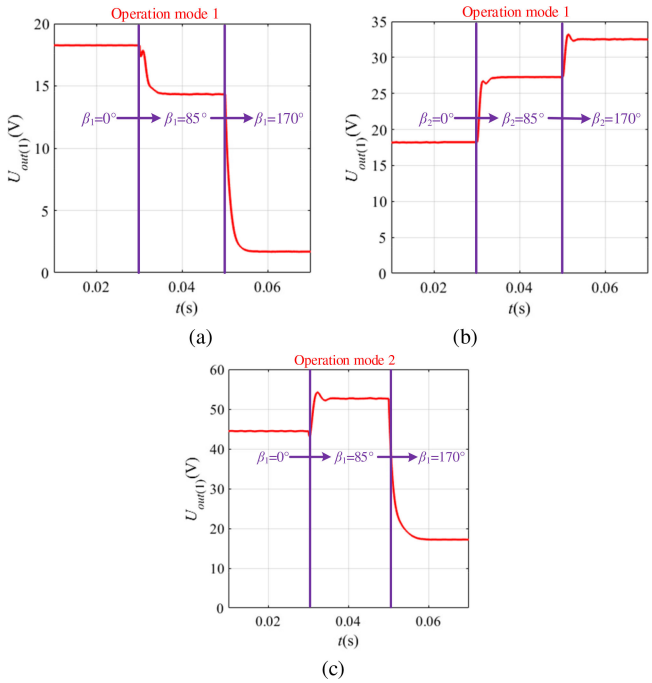

Fig. 24. Dynamic output voltage regulation performance analysis. (a) Variation of $U_{\mathrm{out}(1)}$ with β_1 in operation mode 1. (b) Variation of $U_{\mathrm{out}(1)}$ with β_2 in operation mode 1. (c) Variation of $U_{\mathrm{out}(1)}$ with β_1 in operation mode 2.

In operation mode 1, as can be seen from Fig. 23(a), when both β_1 and β_2 vary from 0° to 180°, the range of the output voltage $U_{\mathrm{out}(1)}$ is 0–60 V. In operation mode 2, as can be seen from Fig. 23(b), when β_1 varies from 0° to 180°, the range of the output voltage $U_{\mathrm{out}(1)}$ is 0–70 V.

To demonstrate the dynamic regulation performance with β_1 and β_2, the regulation response is given in Fig. 24.

As can be seen from Fig. 24, under the regulation of the active rectifier, when β_1 and β_2 change from 0° to 85° and then to 170°, the transition time is less than 5 ms, and the overshoot on the output voltage is less than 2%. Therefore, the transition process is stable, and there is almost no overshoot on the output voltage.

The output voltage regulation performance in two operation modes is listed in Table IV.

As can be seen from Table IV, in operation mode 1, when β_1 changes from 0° to 85° and then to 170°, the range of $U_{\mathrm{out}(1)}$ is 1.7–18.2 V. When β_2 changes from 0° to 85° and then to 170°, the range of $U_{\mathrm{out}(1)}$ is 18.2–32.5 V. In operation mode 2, when β_1 changes from 0° to 85° and then to 170°, the range of $U_{\mathrm{out}(1)}$ is 17.2–44.5 V. Therefore, with the active rectifier, we can realize output voltage regulation to correct dynamic parameters tolerance influence and maintain the output stable.

TABLE IV
OUTPUT VOLTAGE REGULATION PERFORMANCE IN TWO OPERATION MODES

	β_1 (°)	β_2 (°)	$U_{out(1)}$ (V)
Operation mode 1	0	0	18.2
	85	0	14.3
	170	0	1.7
	0	0	18.2
	0	85	27.3
	0	170	32.5
Operation mode 2	0		44.5
	85		52.7
	170		17.2

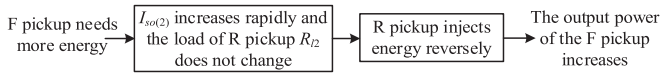

Fig. 25. Process of determining whether the F pickup needs more energy.

E. Method of Determining Whether the F Pickup Needs Energy

In the proposed system, the current track circuit in the pickup is not only used to control the synchronization of multiple sources, but also to determine whether the F pickup needs more energy.

The evaluation process of whether the F pickup needs more energy is shown in Fig. 25. In the operation mode 1, when the F pickup needs more energy, the load of the F pickup R_{l1} will decrease. The current $I_{so(2)}$ in the R pickup can be given by

$$\dot{I}_{so(2)} = \frac{\dot{U}_{\mathrm{ac}} M M_2}{L_p L_{so(2)} \left(\frac{M_1^2 R_{l(1)}}{L_{so(1)}^2} + \frac{M_2^2 R_{l(2)}}{L_{so(2)}^2} \right)}. \tag{49}$$

Equation (49) indicates that $I_{so(2)}$ increases with the decrease of $R_{l(1)}$. When $I_{so(2)}$ is detected to increase rapidly while $R_{l(2)}$ maintains unchanged, it indicates that F pickup needs more energy and R pickup needs to inject energy reversely.

VIII. CONCLUSION

This article proposes a power transfer capability strengthening method for multiple pickups with sharing power channel within a long track coil. The experimental results show that the transient excess power requirement of one pickup can be delivered from the other pickup without increasing the primary power rating. This improves the cost-effectiveness with reduced energy waste. In addition, the proposed synchronization method has been verified to maintain the primary and the reverse injection pickup in phase at a high operating frequency. A boundary condition is set to ensure the power can be reversely inject in strengthening mode. The effects of the mutual inductances and the loads on the system performance are analyzed. Furthermore, the proposed

method can be used in multiple modules if energy sharing is needed between them.

REFERENCES

[1] X. Dai, J. Jiang, and J. Wu, "Charging area determining and power enhancement method for multi-excitation unit configuration of wirelessly dynamic charging EV system," *IEEE Trans. Ind. Electron.*, vol. 66, no. 5, pp. 4086–4096, Jul. 2018.

[2] X. Dai, X. Li, Y. Li, and P. A. Hu, "Maximum efficiency tracking for wireless power transfer systems with dynamic coupling coefficient estimation," *IEEE Trans. Power Electron.*, vol. 65, no. 10, pp. 5005–5015, Jul. 2017.

[3] M. R. Basar, M. Y. Ahmad, J. Cho, and F. Ibrahim, "An improved wearable resonant wireless power transfer system for biomedical capsule endoscope," *IEEE Trans. Ind. Electron.*, vol. 66, no. 5, pp. 7772–7781, Oct. 2018.

[4] L. Li, H. Liu, H. Zhang, and W. Xue, "Efficient wireless power transfer system integrating with metasurface for biological applications," *IEEE Trans. Ind. Electron.*, vol. 65, no. 4, pp. 3230–3239, Apr. 2017.

[5] Z. H. Wang, Y. P. Li, Y. Sun, C. S. Tang, and X. Lv, "Load detection model of voltage-fed inductive power transfer system," *IEEE Trans. Power Electron.*, vol. 28, no. 11, pp. 5233–5243, Nov. 2013.

[6] C. C. Huang, C. L. Lin, and Y. K. Wu, "Simultaneous wireless power/data transfer for electric vehicle charging," *IEEE Trans. Ind. Electron.*, vol. 64, no. 1, pp. 682–690, Jan. 2016.

[7] H. Zeng, S. Yang, and F. Z. Peng, "Design consideration and comparison of wireless power transfer via harmonic current for PHEV and EV wireless charging," *IEEE Trans. Power Electron.*, vol. 32, no. 8, pp. 5943–5952, Aug. 2017.

[8] W. Y. Lee *et al.*, "Finite-Width magnetic mirror models of mono and dual coils for wireless electric vehicles," *IEEE Trans. Power Electron.*, vol. 28, no. 3, pp. 1413–1428, Mar. 2013.

[9] S. Y. Choi, S. Y. Jeong, B. W. Gu, G. C. Lim, and C. T. Rim, "Ultraslim S-Type power supply rails for roadway-powered electric vehicles," *IEEE Trans. Power Electron.s*, vol. 30, no. 11, pp. 6456–6468, Jun. 2015.

[10] C. Park, S. Lee, S. Y. Jeong, G. Cho, and C. T. Rim, "Uniform power I-Type inductive power transfer system with DQ-Power supply rails for on-line electric vehicles," *IEEE Trans. Power Electron.*, vol. 30, no. 11, pp. 6446–6455, Nov. 2015.

[11] S. Cui, Z. Wang, and L. Song, "A novel magnetic coupling mechanism for dynamic wireless charging system for electric vehicles," in *Proc. Veh. Power Propulsion Conf.*, 2016, pp. 1–5.

[12] S. Choi, J. Huh, W. Y. Lee, S. W. Lee, and C. T. Rim, "New cross-segmented power supply rails for roadway-powered electric vehicles," *IEEE Trans. Power Electron.*, vol. 28, no. 12, pp. 5832–5841, Dec. 2013.

[13] M. Budhia, J. T. Boys, G. A. Covic, and C. Y. Huang, "Development of a single-sided flux magnetic coupler for electric vehicle IPT charging systems," *IEEE Trans. Ind. Electron.*, vol. 60, no. 1, pp. 318–328, Jun. 2012.

[14] A. Zaheer, H. Hao, G. A. Covic, and D. Kacprzak, "Investigation of multiple decoupled coil primary pad topologies in lumped IPT systems for interoperable electric vehicle charging," *IEEE Trans. Power Electron.*, vol. 30, no. 4, pp. 1937–1955, Apr. 2015.

[15] Z. Chen, W. Jing, X. Huang, L. Tan, and W. Wang, "A promoted design for primary coil in Roadway-powered system," *IEEE Trans. Magn.*, vol. 51, no. 11, Nov. 2015, Art. no. 8402004.

[16] M. Fu, T. Zhang, X. Zhu, P. C. Luk, and C. Ma, "Compensation of cross coupling in multiple-receiver wireless power transfer systems," *IEEE Trans. Ind. Informat.*, vol. 12, no. 2, pp. 474–482, Apr. 2016.

[17] L. Sun, H. Tang, and S. Zhong, "Load-independent output voltage analysis of multiple-receiver wireless power transfer system," *IEEE Antennas Wireless Propag. Lett.*, vol. 15, pp. 1238–1241, 2016.

[18] D. Ahn and S. Hong, "Effect of coupling between multiple transmitters or multiple receivers on wireless power transfer," *IEEE Trans. Ind. Electron.*, vol. 60, no. 7, pp. 2602–2613, May 2013.

[19] J. Cheng, S. Yue, W. Zhihui, and C. S. Tang, "Multi-load mode analysis for electric vehicle wireless supply system," *Energies*, vol. 11, no. 8, Jul. 2018, Art. no. 1925.

[20] U. K. Madawala and D. J. Thrimawithana, "A bidirectional inductive power interface for electric vehicles in V2G systems," *IEEE Trans. Ind. Electron.*, vol. 58, no. 10, pp. 4789–4796, Oct. 2011.

[21] U. K. Madawala and J. Thrimawithana, "A modular based inductive power transfer system for high power applications," *IET Trans. Power Electron.*, vol. 5, no. 7, pp. 1119–1126, 2012.

Xin Dai (Member, IEEE) received the B.S. degree in industrial automation from Yuzhou University, Chongqing, China, in 2000, and the Ph.D. degree in control theory and control engineering from the School of Automation, Chongqing University, Chongqing, China, in 2006.

In 2012, he was a Visiting Scholar with The University of Auckland, New Zealand. He is currently working as a Professor with the School of Automation, Chongqing University. His current research interests include inductive power transfer technology and nonlinear dynamic behavior analysis of power electronics.

Jinde Wu received the B.S. degree from the College of Information Engineering, Taiyuan University of Technology, Taiyuan, China, in 2015. He is currently working toward the Ph.D. degree in control theory and control engineering with Chongqing University, Chongqing, China.

His current research interests include the bidirectional wireless power transfer and power electronics.

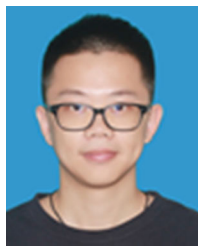

Jincheng Jiang received the B.S. degree from the College of Optoelectronic Engineering, Chongqing University of Posts and Telecommunications, Chongqing, China, in 2015. He is currently working toward the Ph.D. degree in control theory and control engineering with Chongqing University, Chongqing.

His current research interests include the dynamic wireless charging system and multiexcitation units wireless power transfer systems.

Ruozhong Gao received the B.S. and M.Sc. degrees in electrical engineering from the Taiyuan University of Technology, Taiyuan, China, in 2013 and 2017, respectively. He is currently working toward the Ph.D. degree in control theory and control engineering with Chongqing University, Chongqing, China.

His current research interests include the wireless power transfer and power electronics.

Udaya K. Madawala (Fellow, IEEE) received with B.Sc. (hons.) degree in electrical engineering from The University of Moratuwa, Moratuwa, Sri Lanka, in 1987, and the Ph.D. degree in power electronics from The University of Auckland, Auckland, New Zealand, in 1993, as a Commonwealth Doctoral Scholar.

He was employed by Fisher & Paykel Ltd, New Zealand, as a Research and Development Engineer to develop new technologies for motor drives. In 1997, he joined the Department of Electrical and Computer Engineering, The University of Auckland, where he is currently a Full Professor. His research interests include the fields of wireless power transfer, power electronics, V2G applications, and renewable energy.

Dr. Madawala is a Distinguished Lecturer of the IEEE Power Electronic Society (PELS), and has more than 30 years of both industry and research experience in the fields of power electronics and energy. He has served both the IEEE Power Electronics and Industrial Electronics Societies in numerous roles, relating to editorial, advisory, conference, technical committee and chapter activities. He is currently an Associate Editor for IEEE TRANSACTIONS ON POWER ELECTRONICS, and a Member-at-Large of the Administrative Committee and the Oceania Liaison Chair of Membership Development Committee of the IEEE Power Electronics Society. He was the General Chair of the 2nd IEEE Southern Power Electronics Conference (SPEC)-2016, held in New Zealand, and is currently the Chair of the SPEC Steering Committee.